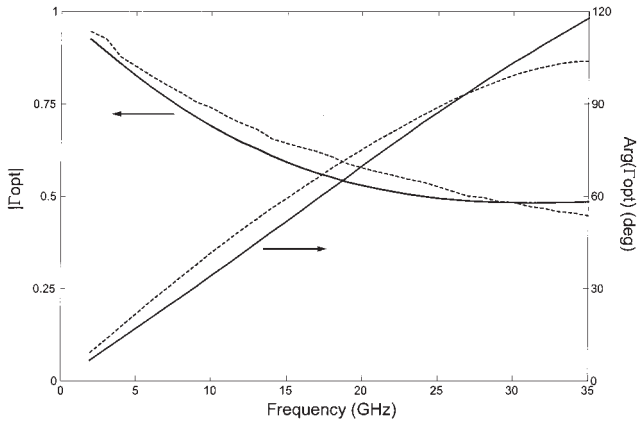

Figure 9 Magnitude and phase of the optimum source reflection coefficient of the NEC 321000 HEMT biased at $V_{ds} = 2$ V and $I_{ds} = 10$ mA, extracted using the proposed method (dashed line) and a method based on [5, 6] (solid line)

tured by NEC, have been extracted for different bias conditions. To this purpose, the device *S*-parameters have been measured up to 40 GHz using an HP8510C vector network analyzer. The F_{50} measurements [12, 13] in the same frequency range have been performed using an on-wafer noise-measurement test bench composed by an NC-346 KA noise source, an HP8970B noise-figure meter, an HP8971C noise-figure test set, and, to extend the measurement frequency up to 40 GHz, a homemade SSB noise-figure test set.

The results obtained at $V_{DS} = 2$ V, $I_D = 10$ mA (corresponding at 25% of I_{DSS}) are as follows. The values of *Cp* and *N* resulting from the noise characterization of the device are shown in Figure 7, and the low-frequency mean value of *Cp* and a value corresponding to a deviation of −5% are also shown. As can be observed from this figure, a frequency limit close to 30 GHz results for the extracted noise model. At higher frequencies, the effects of the device parasitics appear clearly, thus invalidating the assumed approximations. The results of the proposed procedure have been compared with those obtained utilizing a more conventional extraction technique based on [5, 6]. Figures 8 and 9 show the comparison of the results at the considered bias point. Good agreement is observed between the two methods up to 29 GHz, thus confirming the previously determined frequency limitation. In particular, differences lower than 0.1 dB for F_{min}, 1.5Ω for R_n, 0.05° and 10° for magnitude and phase Γ_{opt}, respectively, result in this frequency range. Such results prove the validity of the proposed approach.

CONCLUSION

A method to determine the noise parameters of microwave field-effect transistors has been proposed. The method applies to microwave noise characterization of devices presenting low parasitic effects, in particular, coplanar devices. It makes use of device *Y*-parameters and F_{50} measurements only and does not require extraction of the small-signal equivalent circuit; therefore, it represents a fast and reliable tool for noise modeling of microwave active devices. To take the frequency limitations of the method into account, a criterion to determine the range of validity of the extracted noise parameters has been defined. The proposed technique has been applied to the modeling of a coplanar low-noise HEMT manufactured by NEC, and has been validated via comparison with a more conventional method. Good results are achieved up to 29 GHz, thus proving the validity of the proposed approach.

REFERENCES

1. R.Q. Lane, The determination of device noise parameters, Proc IEEE 57 (1969), 1461–1462.
2. G. Caruso and M. Sannino, Computer-aided determination of microwave two-port noise parameters, IEEE Trans Microwave Theory Tech 26 (1978), 639–642.
3. R.A. Pucel, H.A. Haus, and H. Statz, Signal and noise properties of GaAs microwave FET, Adv Electronics Electron Phys 38 (1975).
4. M.S. Gupta and P.T. Greiling, Microwave noise characterisation of GaAs MESFET's: Determination of extrinsic noise parameters, IEEE Trans Microwave Theory Tech 36 (1988), 745–751.
5. M.W. Pospieszalski, Modelling of noise parameters of MESFETs and MODFETs and their frequency and temperature dependence, IEEE Trans Microwave Theory Tech 37 (1989), 1340–1350.
6. P.J. Tasker, W. Reinert, B. Hughes, J. Braunstein, and M. Schlechtweg, Transistor noise parameter extraction using a 50Ω measurement system, IEEE Int Microwave Symp, Atlanta, GA, 1993, pp 1251–1254.
7. G. Dambrine, J.M. Belquin, F. Danneville, and A. Cappy, A new extrinsic equivalent circuit of HEMTs including noise for millimeter-wave circuit design, IEEE Trans Microwave Theory Tech 46 (1998), 1231–1236.
8. H. Hillbrand and P.H. Russer, An efficient method for computerized noise analysis of linear amplifier networks, IEEE Trans Circ Syst CAS-23 (1976), 235–238.
9. A. Van Der Ziel, Thermal noise in field-effect transistors, Proc IRE, 1962, pp 1808–1812.
10. A. Van Der Ziel, Gate noise in field effect transistors at moderately high frequencies, Proc IEEE (1963), 461–467.
11. J. Lange, Noise characterization of linear two port in terms of invariant parameters, IEEE J Solid-State Circ SC-2 (1967), 37–40.
12. J. Randa, Noise temperature measurements on wafer, NIST Technical Note 1390, 1997.
13. A. Rodriguez, L. Dunleavy, and P. Kirby, Best practice for on-wafer millimeter wave noise figure measurements, 57th ARFTG Conf, Phoenix, AZ, May, 2001.

ELECTROMAGNETIC SIMULATIONS OF METALLIC MATERIALS USING THE MAPPED FOURIER PSTD ALGORITHM

Xiang Gao,[1,2] Mark S. Mirotznik,[3] and Dennis W. Prather[1]
[1] Department of Electrical & Computer Engineering
University of Delaware
Newark, DE 19716
[2] KLA-Tencor
San Jose, CA
[3] Department of Electrical Engineering and Computer Science
The Catholic University of America
Washington, DC 20064

Received 30 August 2004

ABSTRACT: *Previously, the regular Fourier pseudospectral time-domain (PSTD) algorithm was recognized as mainly applicable to simulations of low-contrast dielectric materials. In this paper, we discuss the difficulties in simulating high-contrast and particularly metallic materials using the Fourier PSTD method. To overcome these difficulties, we use a nonuniform grid obtained from a specially designed mapping curve that can reduce the Gibbs phenomenon in the mapped space. The convergence property of this technique is then examined. We show dramatic improvements compared with regular Fourier PSTD and finite-difference time-domain (FDTD) meth-*

ods on a uniform grid. As an example application, we apply our method to the modeling of the 2D scattering of a chrome-projection lithography mask.
 Microwave Opt Technol Lett 44: 569–575, 2005; Published online in Wiley InterScience (www.interscience.wiley.com). DOI 10.1002/mop.20699

Key words: *mapped pseudospectral time-domain algorithm; nonuniform grid; photo mask; Blackman–Harris function; Gibbs phenomenon*

1. INTRODUCTION

The pseudospectral method was first proposed in the 1970s to numerically solve partial-differential equations [1–4]. In the pseudospectral method, first based on some prior knowledge of the solution, a set of basis functions and a set of collocation points are chosen and then the solution sampled at the collocation points is used to determine the projection of the solution onto the basis functions. With the expansion coefficient determined, spatial derivatives can be obtained analytically in the spectral domain, and a regular time-marching scheme can be applied as common time-domain techniques. This method is intrinsically linked to Galerkin's spectral method [4, 5]. With the right set of collocation points, the pseudospectral method is equivalent to Galerkin's method, yet with much simplified numerical operations. Ideally, the pseudospectral method is able to achieve spectral accuracy with a computational complexity similar to a high-order finite-difference method. More recently, the pseudospectral method was also applied to electromagnetic problems [6–21].

In the area of computational electromagnetics, there are primarily two broad categories of pseudospectral methods, depending on the choice of basis functions. One is the Fourier pseudospectral time-domain (PSTD) method [6–18], which assumes a periodic boundary condition and uses the trigonometric Fourier series as the basis functions. The other is the so-called multidomain PSTD [19–21], which uses the Chebyshev or Legendre polynomials defined in a closed domain as the basis functions [4]. In the multidomain approach, the material boundary coincides with the subdomain boundary through a spatial mapping in order to avoid the Gibbs phenomenon [3]. Within each subdomain, the material property is assumed uniform. A patching scheme is applied between neighboring subdomains to properly account for the boundary condition and the continuity of inward and outward propagating fields. Typically, a standard Runge–Kuta scheme is used for time marching. In the former case, namely, the Fourier PSTD method, a uniform grid is typically used in conjunction with perfectly matched layers (PMLs) [22] to eliminate the wrapped-around effect due to the implicit periodic boundary condition in the Fourier series. Along these lines, Fourier PSTD has been successfully applied to low-contrast and low-loss materials, or materials whose EM properties change smoothly. In dielectric materials, the tangential field components are continuous even when the material property is discontinuous along the longitudinal direction. This yields 2nd-order accuracy for the Fourier PSTD method when applied to dielectric materials. In applications when the material contrast is not very large, Fourier PSTD is able to achieve accuracy comparable to that of the FDTD method, however, with a much smaller sampling rate. Unfortunately, when good conductors are involved, the field abruptly changes beneath the conductor surface within a short distance, which can be characterized by skin depth. When the skin depth is much smaller than the cell size used in the PSTD method, this creates high-spatial-frequency components that are not resolved, and consequently yields a strong Gibbs phenomenon. In some cases, nonphysical error waves can visibly contaminate the results.

Due to the omnipresence of the Gibbs phenomenon in numerical modeling using spectral and pseudospectral techniques, there has been extensive research on removing the Gibbs phenomenon when the coefficients in partial-differential equations are discontinuous. But until now, the success has been limited to very few special cases [23–28]. Efficiently removing the Gibbs phenomenon for Maxwell's equations (or hyperbolic equations in general), at every time step is still a daunting task, due to the presence of global basis functions. Current research efforts are more focused on the multidomain pseudospectral method, which separates the computation domains along the material interface in order to avoid the Gibbs phenomenon. A patching condition is used to correctly connect the fields at neighboring domains at each time step. It should be pointed out that the patching conditions remain a frontier of active research [4].

The Gibbs phenomenon, found when analyzing metallic materials using the Fourier PSTD method, has two primary causes. One is that the field changes abruptly beneath the metal surface and, secondly, the solution itself is singular at the interface. (In this paper, we use the term "singular" for solutions that are discontinuous or whose derivatives are discontinuous.) Since the initial appearance of the Fourier PSTD algorithm, it has been suggested that using a nonuniform grid might help resolve the Gibbs phenomenon [9] and offer a better handling of the interface. Recently, the space-transformation or mapping technique was applied to Fourier PSTD, using 2nd-order polynomials as the mapping curve [11, 12]. It should be pointed out that the mapping concept in the pseudospectral method is not new [29]. But previous applications of the mapping technique were primarily for reducing the staircase errors and resolving the abrupt field changes by using a locally dense grid [12, 17]. In this paper, we develop a special mapping technique based on the Blackman–Harris function that not only eliminates the staircase error, but also can precisely control the singularity of the solution on the mapped space and thus suppress the Gibbs phenomenon. With this mapping technique, the mapped PSTD can correctly simulate metallic and high-contrast materials. To illustrate our technique, we study how electromagnetic waves propagate through a chrome mask. This is of great interest for improving the resolution of photolithography processes, as the critical feature sizes of integrated circuits become comparable to the exposure wavelength.

The following section describes how the mapping curve is generated and how the Gibbs phenomenon is reduced with the mapped PSTD.

2. THE MAPPING CURVE AND ITS RESOLVE ON THE GIBBS PHENOMENON

Electromagnetic-field penetration into metallic materials can be described by the skin depth. The electric field inside a metallic material undergoes an exponential attenuation as it penetrates through the surface of a metallic material [30]. To illustrate this point, we consider a normally incident plane wave propagating from a dielectric material (medium 1) onto the flat surface of a metallic material (medium 2). The surface is perpendicular to the z-axis and located at $z = 0$. Suppose the incident fields are given by

$$E^i = \hat{x} E_0 e^{-ik_1 z}, \quad H^i = \hat{y} \frac{E_0}{\eta_1} e^{-ik_1 z}. \tag{1}$$

Then, in medium 1, the total fields can be derived as [30]:

$$E^1 = \hat{x}E_0 e^{-ik_1 z}\left[1 + \left(\frac{\eta_2 - \eta_1}{\eta_2 + \eta_1}\right)e^{i2k_1 z}\right],$$

$$H^1 = \hat{y}\frac{E_0}{\eta_1}e^{-ik_1 z}\left[1 - \left(\frac{\eta_2 - \eta_1}{\eta_2 + \eta_1}\right)e^{i2k_1 z}\right]. \quad (2)$$

Similarly, the fields in medium 2 are given by

$$E^2 = \hat{x}\left(\frac{2\eta_2}{\eta_2 + \eta_1}\right)E_0 e^{-\alpha z}e^{-ik_2 z}, \quad H^2 = \hat{y}\left(\frac{2\eta_2}{\eta_2 + \eta_1}\right)\frac{E_0}{\eta_2}e^{-\alpha z}e^{-ik_2 z}. \quad (3)$$

In Eqs. (2) and (3), η_1 and η_2 are the intrinsic impedance of medium 1 and medium 2, respectively, and α is the attenuation constant in medium 2. It can be verified easily that the tangential field components $E^{1,2}$ and $H^{1,2}$ are continuous, however, their 2nd- or higher-order derivatives are not continuous. Thus, the solution is singular at the interface. This observation is generally true, independent of the incident angle or material geometry. Moreover, because for good conductors the skin depth is very small compared to wavelength, the strong attenuation creates a sharp change in field values, and thus a very high sampling rate is required to ensure accurate modeling of the interface. However, this sharp change of field component is only a local phenomenon. Therefore, we can use a locally denser nonuniform grid to resolve the sharp changes. In addition, when this nonuniform grid is constructed correctly, it can reduce the singularity of the solution and, in turn, reduce the Gibbs phenomenon, as explained in the following section.

Suppose we have a function $f(x)$, that is continuous but has a singular point at $x = x_0$. We can choose a mapping curve $x(u)$ to map $x_i \in \mathbf{R}$ onto a uniform grid $u_i \in \mathbf{R}$, such that

$$\frac{df(x)}{du} = \frac{dx}{du}\frac{df(x)}{dx}. \quad (4)$$

The jump of df/dx due to the singularity at point x_0 is scaled by dx/du, which is a small number for a locally dense grid. Higher-order derivatives are scaled by dx/du and higher-order derivatives of x on u as well. For example,

$$\frac{d^2f}{du^2} = \frac{d^2f}{dx^2}\left(\frac{dx}{du}\right)^2 + \frac{df}{dx}\frac{d^2x}{du^2}. \quad (5)$$

Thus, if forward and inverse fast Fourier transforms (FFT/iFFTs) [31–32] are used to obtain the derivatives of df/du, the Gibbs phenomenon can be suppressed (this is the connection between the Gibbs phenomenon and a mapping curve). In this paper, we use the mapping technique to suppress the Gibbs phenomenon. For this purpose, we developed a method of constructing mapping curves based on Blackman–Harris window functions that precisely controls the value of dx/du at the singular points x_0. Also, our method can eliminate the staircase error for rectangular geometries.

For a uniform grid, the $x(u)$ transformation curve is a straight line, which can be written as $q(u) = uh + const.$ We define $h = L/N$ as the changes in x_i when the transformation curve is a straight line. The ideal mapping curve should pass through the (x_0, u_0) point, where u_0 is an integer. In this way, the interface located at x_0 will not have staircase error on the nonuniform grid. We introduce $w(u) = x(u) - q(u)$ (see Fig. 1). Then, dx/du is given by

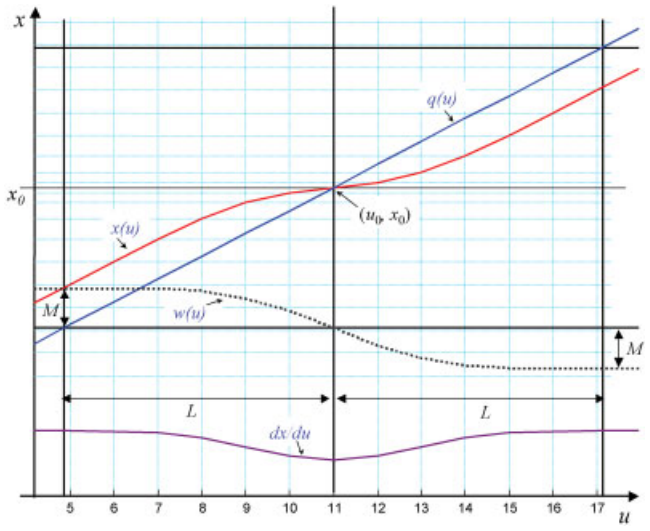

Figure 1 Construction of a smooth transformation curve $x(u)$. [Color figure can be viewed in the online issue, which is available at www.interscience.wiley.com.]

$$\frac{dx}{du} = \frac{dw}{du} + \frac{dq}{du} = \frac{dw}{du} + h. \quad (6)$$

Suppose $w(u)$ is constructed from the following formula:

$$w(u) = 2M \cdot IBH\left(\frac{u}{2L}\right), \quad (7)$$

where $IBH(x)$ is the integral form of the so-called Blackman–Harris (BH) window function [16] and is defined within [0 1] and smoothly connects 0 and 1 [16]. Here, we use M and L to scale $IBH(x)$ in the x and u directions, as shown in Figure 1. Also, recall that the derivative of $IBH(x)$ is given by $BH(x)$. These two functions can be written as

$$IBH(x) = \sum_{k=0}^{Q} a_k \frac{\sin(2\pi kx)}{2\pi k}, \quad BH(x) = \sum_{k=0}^{Q} a_k \cos(2\pi kx), \quad (8)$$

where x is within [0 1] and $Q + 1$ is the number of terms for the BH window function. In our examples, we use $Q = 3$, $a_0 = 1.0$, $a_1 = -1.3611$, $a_2 = 0.3938$, and $a_3 = -0.0326$, which are obtained by normalizing the -92-dB BH coefficients a_k to a_0. This insures that $IBH(0) = 0$ and $IBH(1) = 1$. Then we obtain

$$\frac{dx}{du} = \frac{M}{L}BH\left(\frac{u}{2L}\right) + h. \quad (9)$$

If we choose to have the singular point located in the center of the BH window function, as shown in Figure 1, then dx/du at the singular point becomes

$$\tau = \left.\frac{dx}{du}\right|_{center} = \frac{M}{L}BH(1/2) + h = 2.78746\frac{M}{L} + h. \quad (10)$$

So it is clear that once h, τ, and M are given, then L can be uniquely determined from Eq. (10). Once M and L are defined, $w(u)$ is uniquely determined [see Eq. (7)]. The $w(u)$ curve is then padded with constants that are equal to the values at its end points,

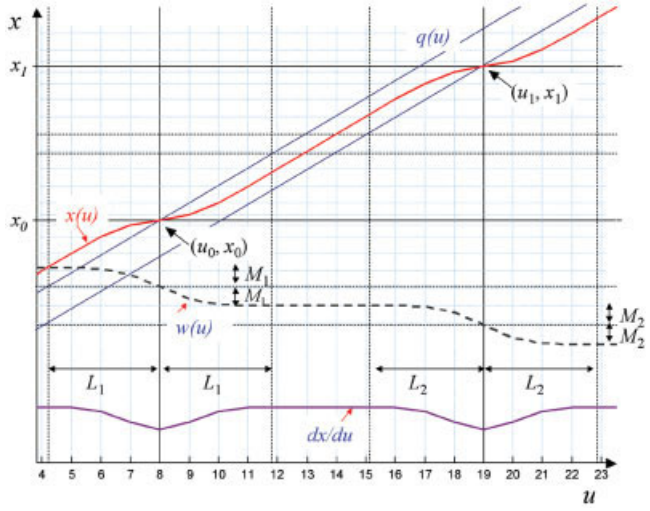

Figure 2 Construction of $x(u)$ when there is more than one singular point. [Color figure can be viewed in the online issue, which is available at www.interscience.wiley.com.]

as shown by the $w(u)$ curve in Figure 1. Once $w(u)$ is obtained, $x(u)$ and dx/du are available.

When there is more than one interface $\{x_i\}$ along the x-axis, we can sum up all individual $w_i(u)$ curves as the final $w(u)$ curve (see Fig. 2). If there are no staircase errors for interface x_0 and x_1 on the mapped grid, then we obtain

$$x_2 - x_1 = w(u_2) - w(u_1) + (u_2 - u_1)h = M_1 + M_2 + (u_2 - u_1)h. \quad (11)$$

Because u_1 and u_2 are integers, Eq. (11) requires $\mathrm{mod}(x_2 - x_1 - (M_1 + M_2), h) = 0$. This ensures that once $x(u)$ passes through (x_0, u_0), it will pass through (x_1, u_1) as well. In general, for more than one interface whose locations are defined by a vector $\{x_i\}$, the following procedures are applied:

1. define h, τ, and the expected average value of $\{M_i\}$;
2. from $\{x_i\}$, seeking M_i that ensures that $\mathrm{mod}(x_i - x_{i+1} - (M_i + M_{i+1}), h) = 0$, also minimize the standard deviation of $\{M_i\}$ whose average value should be close to the target value set in step 1;
3. from h, τ, and $\{M_i\}$, determine $\{L_i\}$, and also the $w_i(u)$ curve, such that summing up all individual $w_i(u)$ curves results in the final $w(u)$ curve;
4. add $w(u)$ with $q(u)$, and align the resultant $x(u)$ with one of the interfaces, such that the rest of the interfaces will fall onto the nonuniform grid;
5. obtain the dx/du curve analytically, which is done by simply adding all dw_i/du curves and the constant h.

The above procedures were realized in less than 100 lines of Matlab code and required less than a second to execute. Also note that this mapping procedure is only executed once for each dimension and the results are stored for the entire simulation.

Once the $x(u)$ transformation curve is obtained, the nonuniform grid $\{x_n\}$ and dx/du at $\{x_n\}$ are easily obtained. (Throughout this letter, we use $\{x_i\}$ to represent the interface location and $\{x_n\}$ to represent the coordinate of the nonuniform grid.) We can then proceed to use the mapped PSTD algorithm directly [17].

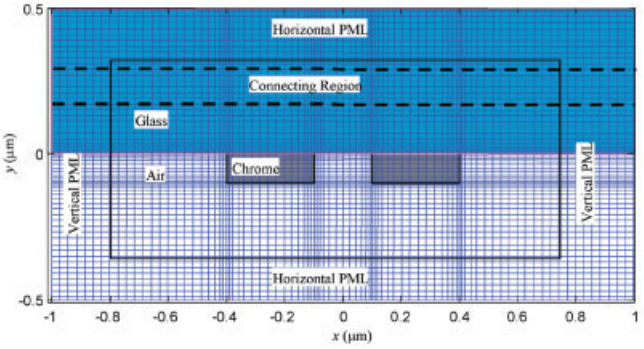

Figure 3 Diagram of the nonuniform grid and the 2D structure of a chrome mask. [Color figure can be viewed in the online issue, which is available at www.interscience.wiley.com.]

To minimize the Gibbs phenomenon that may arise due to dx/du, the dx/du curve should be a very smooth one. In this study, we used the Blackman–Harris function for dx/du [16]. This is the primary reason we choose its integral form for $w(u)$.

3. NUMERICAL RESULTS

To illustrate the usefulness of the mapped Fourier PSTD method, we studied the electromagnetic propagation through a chrome photomask. The mask has a 100-nm-thick chrome layer formed on the surface of a glass substrate assumed to be semi-infinite. The mask is also assumed to have features that are invariant along the z-axis, so that the problem can be treated as a 2D scattering problem. We studied the TM_z mode. The incident field is assumed to be a normally incident plane wave with a wavelength of 200 nm. Because there is no consistent reported conductivity σ for chrome masks, we tested three possible values: 1×10^5 S/m, 1×10^6 S/m, and 1×10^7 S/m.

Figure 3 shows a diagram of the nonuniform grid and mask structures. Figure 4 shows a close-up view of the interfaces, which shows that this nonuniform grid is staircase-error free. The plane-wave soft source is introduced by using the recently developed weighted TF/SF method [16]. The connecting region, which separates the total field and the scattered field, is a "belt" across the computational region (including the two vertical PMLs), as shown by the two dotted lines in Figure 3. This structure works well, since the propagation direction of the incident wave is parallel to the two vertical PMLs. The incident wave can travel in parallel through the vertical PMLs without any loss, and thus will not create errors for normal incident waves. To verify this, we calculated the fields with

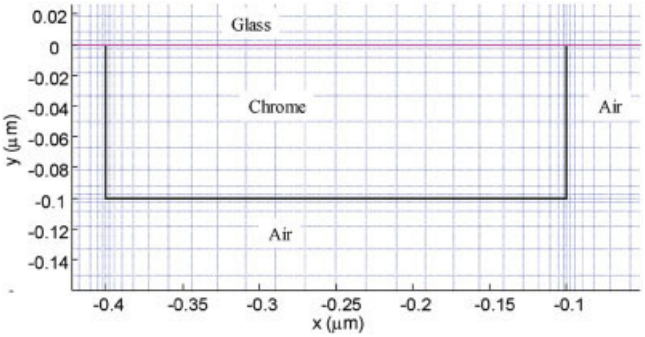

Figure 4 Close-up view of a typical nonuniform grid with $\tau = 0.1$. [Color figure can be viewed in the online issue, which is available at www.interscience.wiley.com.]

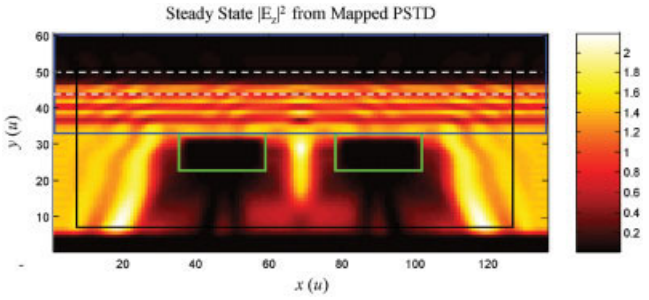

Figure 5 Steady state of E_z on a nonuniform grid with 136 and 60 grid points in the x and y directions, respectively, corresponding to roughly 9 and 8 grids per minimum wavelength in the x and y directions (PML thickness = 8 cells; $\sigma = 1 \times 10^6$ S/m). [Color figure can be viewed in the online issue, which is available at www.interscience.wiley.com.]

the chrome layer removed from the glass substrate. The total field is uniform inside the glass, air, and vertical PML regions, with correct reflection and transmission coefficients. When the chrome layer is present, the PMLs will absorb any nonparallel propagating waves, so that the scattered field due to the chrome layer is absorbed properly. This approach greatly simplified our treatment of the incident plane wave.

Figure 5 shows the steady-state result for the E_z component. Note that the result is plotted on the transformed space, and the field near the interfaces is stretched as a result.

The accuracy and convergence of the mapped PSTD algorithm was also investigated. Figures 6–8 show the convergence property of the mapped PSTD for three possible σ values of the thin chrome layer. In comparison, the same structure is also studied with uniform PSTD and FDTD algorithms. As shown in Figures 6–8, the uniform PSTD falls short of even the standard FDTD method when analyzing metallic materials. This is due to the strong global influence of the Gibbs phenomenon within the PSTD algorithm. However, our mapped PSTD algorithm is able to achieve much better results than the FDTD algorithm. For all the convergence

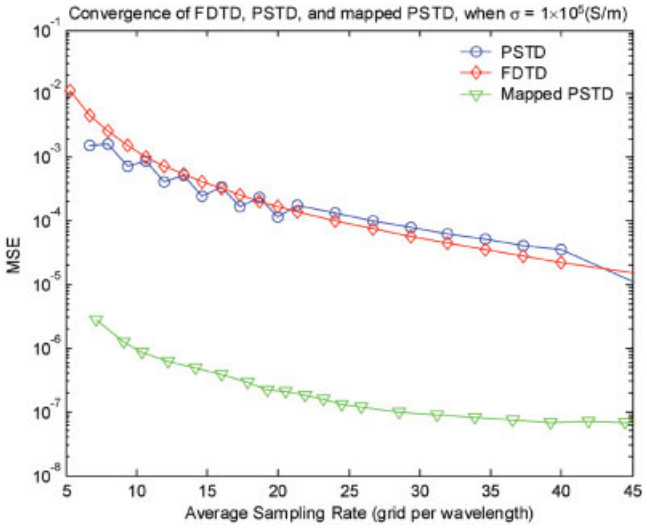

Figure 6 Convergence of FDTD, PSTD, and mapped PSTD on the 2D simulation of a chrome mask with $\sigma = 1 \times 10^5$ S/m, skin depth around 60 nm, and incident wavelength 200 nm. For mapped PSTD, $\tau = 0.1$ and M of about 80 and 40 nm in the x and y directions, respectively, are used to generate the mapping curves. [Color figure can be viewed in the online issue, which is available at www.interscience.wiley.com.]

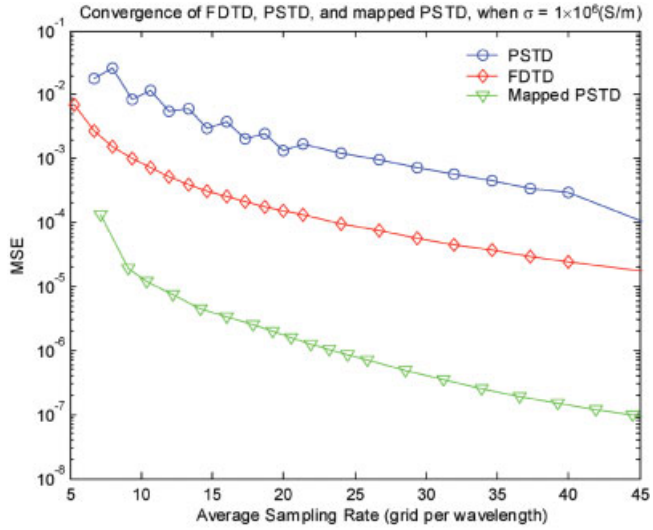

Figure 7 Convergence of FDTD, PSTD, and mapped PSTD on the 2D simulation of a chrome mask with $\sigma = 1 \times 10^6$ S/m, skin depth around 14 nm, and incident wavelength 200 nm. For mapped PSTD, $\tau = 0.1$ and M of about 80 and 40 nm in the x and y directions, respectively, are used to generate the mapping curves. [Color figure can be viewed in the online issue, which is available at www.interscience.wiley.com.]

curves calculated using the mapped PSTD method, the PML thickness was fixed at eight cells and the connecting region thickness was fixed at 12 cells. This is the major reason that the convergence curves become flat at higher sampling rate. The mean square error (MSE) of E_z is obtained in the region $-0.75\ \mu\text{m} < x < 0.75\ \mu\text{m}$ and $-0.30\ \mu\text{m} < y < -0.11\ \mu\text{m}$ (see Figs. 3 and 4), since the near field behind the mask is of primary interest. For the mapped PSTD, the grid is nonuniform in this region and thus has more samples near the material boundary, where the errors tend to be larger. Consequently, the MSE calculation is slightly

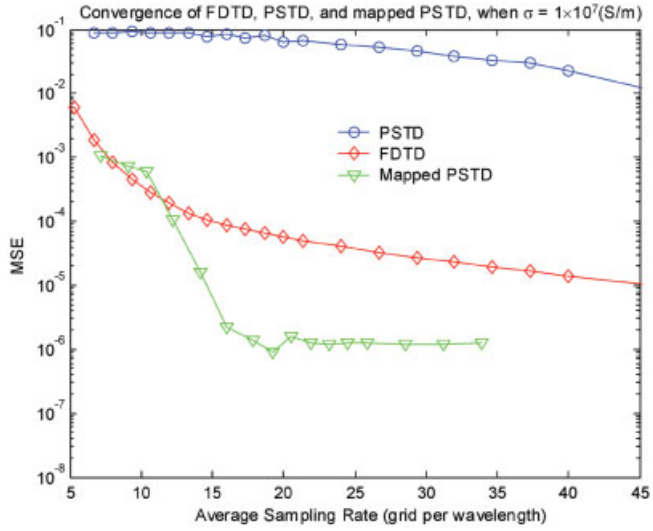

Figure 8 Convergence of FDTD, PSTD, and mapped PSTD on the 2D simulation of a chrome mask with $\sigma = 1 \times 10^7$ S/m, skin depth around 4 nm, and incident wavelength 200 nm. For mapped PSTD, $\tau = 0.01$, and M of about 80 and 80 nm in the x and y directions, respectively, are used to generate the mapping curves (in this particular case, the chrome layer thickness is 200 nm). [Color figure can be viewed in the online issue, which is available at www.interscience.wiley.com.]

more unfavorable for the mapped PSTD algorithm in comparison to the FDTD one. Even so, the mapped PSTD shows a much better MSE. It should also be pointed out that in our convergence study of FDTD and uniform PSTD algorithms, we choose the mask structure and sampling rate such that staircase errors are not encountered; hence, the comparison is fair.

Comparing Figures 6–8, it is clear that the performance of mapped PSTD and standard PSTD begin to degrade as the conductivity σ of the metal layer increases or as the skin depth δ becomes smaller. This can be easily explained by the fact that as the skin depth decreases, it is harder to resolve the abrupt field changes and Gibbs phenomenon becomes larger. It should be pointed out that in Figure 8, where skin depth is only 4 nm, we have to use a smaller τ for the mapping curves to create a grid that is dense enough near the chrome surface. The mask thickness is increased to 200 nm so that the grid can be made more dense in the y direction for this particular case. However, a relatively larger average sampling rate is still required to fully resolve the Gibbs phenomenon, as indicated by the relatively large errors at smaller sampling rates in Figure 8. In cases when the skin depth is extremely small, we believe that the material should be treated like a PEC and a new PSTD algorithm with different basis functions should be used to correctly handle the boundary conditions.

4. DISCUSSION

The regular Fourier PSTD algorithm on a uniform grid suffers from the Gibbs phenomenon due to discontinuities in the material properties. Consequently, the primary success of the Fourier PSTD algorithm has been limited to low-contrast and low-loss dielectric materials. For high-contrast and (in particular) metallic materials, the uniform-grid method will generally fail to resolve the abrupt field variations near a material surface. More importantly, the tangential H fields become discontinuous for very good conductors and a severe Gibbs phenomenon will greatly contaminate the simulation results, yielding only a 1st-order algorithm. A denser grid can help resolve abrupt field variations and, by constructing a proper grid using the presented method, the local singularity is greatly reduced by a value of τ. In general, a small τ value of 0.01–0.1 seems to provide the optimum performance, depending on the sampling rate as well as the metallic materials conductivity. Smaller τ values tend to produce a very dense grid near the boundary, thus requiring a very small time step. Small values of τ should thus be avoided.

There are two major factors that contribute to the superior convergence behavior of the mapped PSTD method presented in this paper. One is that the magnitude of the Gibbs artifact is significantly suppressed with the application of a mapping curve obtained from the Blackman–Harris function. This becomes clear in Figure 6, where the skin depth is not too serious an issue for PSTD, but mapped PSTD is able to achieve much better accuracy even for very small sampling rates. The other factor is that the nonuniform grid can help resolve the sharp field changes near the material surface, without requiring a large number of grid points. When the skin depth is extremely small, however, a larger sampling rate is required to resolve the drastic field changes. This is the main cause of the large errors of mapped PSTD for small sampling rates in Figure 8.

Unlike the multidomain PSTD algorithm, which uses the Gauss–Lobatto collocation points [4] and Chebyshev polynomials as basis functions, our mapped PSTD uses global basis functions, and thus avoids the complicated patching conditions found in the multidomain PSTD algorithm. Interestingly, the distribution of our nonuniform grid looks similar to the Gauss–Lobatto collocation points (see Fig. 4).

In general, for PSTD on a nonuniform grid, the complicated nonuniform FFT algorithm [33–36] needs to be used. However, through the mapping technique, a standard regularly spaced FFT algorithm can be used. In addition, since the mapping curve is calculated only once before time marching begins, this algorithm is very efficient and easy to program based on existing PSTD codes.

The apparent drawback of the mapped PSTD approach is the stringent requirement for an orthogonal grid. This limits applications to thin films and structures that have rectangular geometries. We believe that applying the mapped PSTD in a global curvilinear form may help the modeling of more complicated geometries.

5. CONCLUSION

In this paper, we have discussed the difficulties of using the Fourier-based PSTD algorithm to conduct electromagnetic simulations of structures that contain high-dielectric-contrast and metallic materials. To address these difficulties, we have presented a method to create a spatial mapping curve that can: (i) produce a locally dense grid to resolve the abrupt field changes, (ii) reduce the singularity of the solution on the mapped space, and (iii) eliminate staircase error for rectangular structures. This new technique was applied to the example of electromagnetic-wave propagation through a think chrome mask. The results from the FDTD and PSTD methods and our new mapped PSTD algorithm suggest the superiority of the new technique.

ACKNOWLEDGMENT

X. Gao would like to thank Prof. Tobin A. Driscoll at the University of Delaware for very useful discussions on pseudospectral time-domain techniques.

REFERENCES

1. D. Gottlieb and S.A. Orszag, Numerical analysis of spectral methods, SIAM, Philadelphia, PA, 1977.
2. C. Canuto, M.Y. Hussani, A. Quarteroni, and T. Zang, Spectral Methods in Fluid Dynamics, Springer-Verlag, New York, 1988.
3. B. Fornberg, A practical guide to pseudospectral methods, Cambridge University Press, New York, 1996.
4. J.P. Boyd, Chebyshev and Fourier spectral methods, 2nd ed., Dover Publications, Mineola, NY, 2001.
5. D. Gottlieb and J.S. Hesthaven, Spectral methods for hyperbolic problems, J Computat Appl Mathem 128 (2001), 83–131.
6. Q.H. Liu, The PSTD algorithm: A time-domain method requiring only two cells per wavelength, Microwave Opt Technol Lett 15 (1997), 158–165.
7. Q.H. Liu, PML and PSTD algorithm for arbitrary lossy anisotropic media, IEEE Microwave Guided Wave Lett 9 (1999), 48–50.
8. Q.H. Liu, A frequency-dependent PSTD algorithm for general dispersive media, IEEE Microwave Guided Wave Lett 9 (1999), 51–53.
9. Q.H. Liu, Large-scale simulations of electromagnetic and acoustic measurements using the pseudospectral time-domain (PSTD) algorithm, IEEE Trans Geosci Remote Sensing 37 (1999), 917–926.
10. Y.F. Leung and C.H. Chan, Pseudospectral time-domain (PSTD) method with unsplit-field PML, Microwave Opt Technol Lett 22 (1999), 278–283.
11. W.K. Leung and Y.C. Chen, Transformed-space nonuniform pseudospectral time-domain algorithm, Microwave Opt Technol Lett 28 (2001), 391–396.
12. X.P. Liu and Y.C. Chen, Applications of transformed-space nonuniform PSTD (TSNU-PSTD) in scattering analysis without the use of the non-uniform FFT, Microwave Opt Technol Lett 38 (2003), 16–21.
13. Q.L. Li, Y.C. Chen, and D. Ge, Comparison study of the PSTD and FDTD methods for scattering analysis, Microwave Opt Technol Lett 25 (2000), 220–226.
14. G.X. Fan and Q.H. Liu, Pseudospectral time-domain algorithm applied

to electromagnetic scattering from electrically large objects, Microwave Opt Technol Lett 29 (2001), 123–125.
15. Q.H. Liu and J.Q. He, An efficient PSTD algorithm for cylindrical coordinates, IEEE Trans Antennas Propagat 49 (2001), 1349–1351.
16. X. Gao, M.S. Mirotznik, and D.W. Prather, A method for introducing soft sources in the PSTD algorithm, IEEE Trans Antennas Propagat 52 (2004), 1665–1671.
17. X. Gao, M.S. Mirotznik, S.Y. Shi, and D.W. Prather, Applying a mapped pseudospectral time-domain method in simulating diffractive optical elements, J Optics Soc Am A 21 (2004), 777–785.
18. X. Gao, M.S. Mirotznik, and D.W. Prather, Dispersion compensation techniques for the Fourier PSTD algorithm, Microwave Opt Technol Lett 42 (2004), 357–361.
19. B. Yang, D. Gottlieb, and J.S. Hesthaven, Spectral simulations of electromagnetic wave scattering, J Computat Phys 134 (1997), 216–230.
20. B. Yang and J.S. Hesthaven, Multidomain pseudospectral computation of Maxwell's equations in 3D general curvilinear coordinates, Appl Numer Math 33 (2000), 281–289.
21. G.X. Fan, Q.H. Liu, and J.S. Hesthaven, Multidomain pseudospectral time-domain simulations of scattering by objects buried in lossy media, IEEE Trans Geosci Remote Sensing 40 (2002), 1366–1373.
22. J.P. Berenger, A perfectly matched layer for the absorption of electromagnetic waves, J Computat Phys 114 (1994), 185–200.
23. D. Gottlieb and E. Tadmor, Recovering pointwise values of discontinuous data with spectral accuracy, Progress and supercomputing in computational fluid dynamics, Birkhäuser, Boston, 1984, pp. 357–375.
24. D. Gottlieb and C.W. Shu, On the Gibbs phenomenon V: Recovering exponential accuracy form collocation point values of a piecewise analytic function, Numer Math 71 (1995), 511–526.
25. D. Gottlieb and C.W. Shu, On the Gibbs phenomenon and its resolution, SIAM Rev 39 (1997), 644–668.
26. D. Gottlieb and C.W. Shu, A general theory for the resolution of the Gibbs phenomenon, Tricomi's ideas and contemporary applied mathematics, National Italian Academy of Science, 1997.
27. A. Gelb, A hybrid approach to spectral reconstruction of piecewise smooth functions, J Scientific Comput 15 (2000).
28. A.K. Tornberg and B. Engquist, Regularization techniques for numerical approximation of PDEs with singularities, J Scientific Comput 19 (2003), 527–552.
29. Bayliss and E. Turkel, Mappings and accuracy for Chebyshev pseudospectral methods, J Computat Phys 101 (1992), 342–359.
30. C.A. Balanis, Advanced Engineering Electromagnetics, Wiley, New York, 1989.
31. J.W. Cooley and J.W. Tukey, Algorithm for the machine computation of complex Fourier series, Math Comput 19 (1965), 2977–301.
32. R.N. Bracewell, The Fourier transform and its applications, 2nd ed., McGraw-Hill, New York, 1986.
33. Dutt and V. Rokhlin, Fast Fourier transforms for nonequispaced data, SIAM J Sci Comput 14 (1993), 1368–1393.
34. N. Nguyen and Q.H. Liu, The regular Fourier matrices and nonuniform fast Fourier transforms, SIAM J Sci Comput 21 (1999), 283–293.
35. Q.H. Liu, An accurate algorithm for nonuniform fast Fourier transforms, IEEE Microwave Guided Wave Lett 8 (1998), 18–20.
36. B. Tian and Q.H. Liu, Nonuniform fast cosine transform and Chebyshev PSTD algorithms, Prog Electromagn Res 28 (2000), 253–273.

ENHANCED MICROSTRIP COUPLED-LINE BANDPASS FILTER BY MEANS OF EBG STRUCTURES ON THE MIDDLE LAYER FOR SPURIOUS SUPPRESSION

Min-Hung Weng,[1] Tsung-Hui Huang,[2] and Cheng-Yuan Hung[2]
[1] National Nano Device Laboratories
Tainan, Taiwan
[2] Department of Computer and Communication
SHU TE University
Kaoshsiung, Taiwan

Received 28 August 2004

ABSTRACT: *In this paper, a microstrip parallel-coupled bandpass filter based on electromagnetic bandgap (EBG) structures to achieve spurious suppression is presented. The EBG loops of the middle layer add an extra stopband-rejection mode to the 2nd and 3rd harmonics of the filter with attenuation losses of over than −30 dB, without affecting the center frequency and insertion loss of the originally designed filter.* © 2005 Wiley Periodicals, Inc. Microwave Opt Technol Lett 44: 575–577, 2005; Published online in Wiley InterScience (www.interscience.wiley.com). DOI 10.1002/mop.20700

Key words: *filters; EBG; microstrip; harmonic*

1. INTRODUCTION

Because of its light weight, low cost, and ease of integration, conventional parallel-coupled filters are favorable for use in modern microwave systems. However, the spurious response of parallel-coupled filters usually occurs at two and three times the fundamental frequency due to the half-wavelength of the resonators. Therefore, suppression of the spurious response is an essential issue for conventional half-wavelength or quarter-wavelength microstrip filters. Recently, the application of electromagnetic bandgap (EBG) structures on microwave filters for rejecting spurious responses has attracted much interest [1–4]. Generally speaking, EBG structures are periodic cells that prevent the propagation of electromagnetic waves in a specified band of frequency [1].

For the purposes of broad-stopband characteristics, some microstrip filters have been designed and fabricated using EBG structure [1–3]. For example, T. Itoh et al. has presented the UC-PBG ground plane to suppress the spurious response of microstrip bandpass filter (BPF) with the advantages of low loss and moderate impedance [1]. However, most of the abovementioned PBG structures have holes in the substrate or etched patterns in the ground plane, and therefore the disadvantages of the structures are package problems and the realization of MMICs [2, 3]. Other drawbacks of EBGs are the effect upon the center frequency and the insertion loss of the original designed filter.

In this paper, two types of rectangular EBG loops on the middle layer for the microstrip parallel-coupled BPF are designed and fabricated to avoid the package problem and to achieve the multiple suppressions, as shown in Figure 1. The EBG loops are designed by using the EM simulations and verified by the experimented results. Moreover, the conventional methodology of the filters holds.

2. DESIGN AND EXPERIMENT

The proposed BPF is mainly composed of the conventional parallel-coupled filter on the top layer and two types of EBG loops on the middle layer. To design a Chebyshev-type BPF, the target characteristics of filter are required. The parallel-coupled filter is a